AGU PUBLICATIONS

JGR

Journal of Geophysical Research: Space Physics

RESEARCH ARTICLE
10.1002/2017JA024981

Key Points:
- We study equatorial and low-latitude electrodynamic and ionospheric disturbances that occurred during the 22–23 June 2015 storm
- At the beginning of the storm, the EEJ and low-latitude ionopsheric behavior was driven by the prompt penetration electric fields
- At the end of the storm, thermospheric winds and composition played a significant role in driving a strong positive storm in Asian sector

Supporting Information:
- Supporting Information S1
- Figure S1
- Figure S2

Correspondence to:
E. Astafyeva,
astafyeva@ipgp.fr

Citation:
Astafyeva, E., Zakharenkova, I., Hozumi, K., Alken, P., Coïsson, P., Hairston, M. R., & Coley, W. R. (2018). Study of the equatorial and low-latitude electrodynamic and ionospheric disturbances during the 22–23 June 2015 geomagnetic storm using ground-based and spaceborne techniques. *Journal of Geophysical Research: Space Physics*, *123*, 2424–2440. https://doi.org/10.1002/2017JA024981

Received 10 NOV 2017
Accepted 2 MAR 2018
Accepted article online 6 MAR 2018
Published online 30 MAR 2018

Study of the Equatorial and Low-Latitude Electrodynamic and Ionospheric Disturbances During the 22–23 June 2015 Geomagnetic Storm Using Ground-Based and Spaceborne Techniques

E. Astafyeva[1], I. Zakharenkova[2], K. Hozumi[3], P. Alken[4], P. Coïsson[1], M. R. Hairston[5], and W. R. Coley[5]

[1]Institut de Physique du Globe de Paris, Paris Sorbonne Cité, University Paris Diderot, UMR CNRS 7154, Paris, France, [2]West Department of IZMIRAN, Kaliningrad, Russia, [3]National Institute of Information and Communications Technology, Tokyo, Japan, [4]Cooperative Institute for Research in Environmental Sciences, University of Colorado Boulder, Boulder, CO, USA, [5]The W. B Hanson Center for Space Sciences, University of Texas at Dallas, Richardson, TX, USA

Abstract We use a set of ground-based instruments (Global Positioning System receivers, ionosondes, magnetometers) along with data of multiple satellite missions (Swarm, C/NOFS, DMSP, GUVI) to analyze the equatorial and low-latitude electrodynamic and ionospheric disturbances caused by the geomagnetic storm of 22–23 June 2015, which is the second largest storm in the current solar cycle. Our results show that at the beginning of the storm, the equatorial electrojet (EEJ) and the equatorial zonal electric fields were largely impacted by the prompt penetration electric fields (PPEF). The PPEF were first directed eastward and caused significant ionospheric uplift and positive ionospheric storm on the dayside, and downward drift on the nightside. Furthermore, about 45 min after the storm commencement, the interplanetary magnetic field (IMF) Bz component turned northward, leading to the EEJ changing sign to westward, and to overall decrease of the vertical total electron content (VTEC) and electron density on the dayside. At the end of the main phase of the storm, and with the second long-term IMF Bz southward turn, we observed several oscillations of the EEJ, which led us to conclude that at this stage of the storm, the disturbance dynamo effect was already in effect, competing with the PPEF and reducing it. Our analysis showed no significant upward or downward plasma motion during this period of time; however, the electron density and the VTEC drastically increased on the dayside (over the Asian region). We show that this second positive storm was largely influenced by the disturbed thermospheric conditions.

1. Introduction

It is known that in the equatorial and low-latitude regions the ionospheric plasma distribution and dynamics are controlled by E and *F* region electrodynamic processes (e.g., Fejer, 1981, 2002; Heelis, 2004). During magnetically quiet periods of time, the low-latitude ionosphere is shielded from high-latitude electric field by the action of region 2 field-aligned currents, and the low-latitude electric fields are generated primarily by the neutral wind dynamo. On the dayside, the neutral winds set up a polarization electric field which usually points into the eastward direction; on the nightside, the electric field is directed westward (e.g., Fuller-Rowell, 2011; Heelis, 2004). At the magnetic dip equator, where the magnetic field is horizontal, the dayside zonal electric field causes an upward E × B drift of the electrons, and generates a negative charge at the top and a positive charge at the bottom of the ionospheric *E* region (about 90 to 130 km altitude). The resulting polarization electric field prevents the farther upward drift of electrons. At the same time, the electrons are driven westward by dayside electric field. This westward movement of the electrons constitutes a dayside eastward electric current at the altitude of ~90–130 km which is called the equatorial electrojet (EEJ).

During geomagnetic storms, the equatorial and low-latitude zonal electric fields (EF) change drastically, resulting from two major sources: (1) penetration of high-latitude convection electric fields of magnetospheric origin (called prompt penetration electric fields, PPEF) and (2) disturbance dynamo electric fields (DDEF) caused by storm time neutral winds.

A southward turning of the interplanetary magnetic field (IMF) Bz component initiates a growth of substorm activity and a rapid increase of high-latitude convection. This expansion is faster than the magnetosphere can

respond, so that the high-latitude convection electric fields penetrate into the low-latitude ionosphere (Huang et al., 2007; Huang et al., 2005; Kelley et al., 1979; Kikuchi et al., 2000; Kikuchi & Hashimoto, 2016; Kikuchi et al., 2008; Nishida, 1968). These PPEF have eastward polarity on the dayside and westward on the nightside. The enhanced convection also leads to the buildup of the shielding layer by the region 2 current, so that when the IMF Bz turns northward, an overshielding EF opposite to the PPEF polarity penetrates into low-latitude ionosphere (Fejer et al., 1979; Kelley et al., 1979), and the penetration can be as efficient as during Bz southward periods of time (Manoj et al., 2008; Tsurutani et al., 2008). Huang et al. (2007) estimated the efficiency of PPEF to be about 9.6%.

The DDEF are driven by disturbed thermospheric winds. The storm-time-enhanced high-latitude heating reinforces the meridional neutral winds, producing strong equatorward winds. These disturbance winds generate a westward/eastward electric field on the dayside/nightside at low latitudes, which opposes their quiet-time patterns (e.g., Blanc & Richmond, 1980; Fuller-Rowell et al., 2002; Huang, 2013; Maruyama et al., 2005; Scherliess & Fejer, 1997; Yamazaki & Kosch, 2015). Contrary to the PPEF that act almost immediately, the disturbance dynamo develops more slowly: it takes several hours to set up the disturbance winds and the associated dynamo electric fields, after which they can persist for many hours due to the neutral-air inertia (Maruyama et al., 2005). The effect of the disturbance dynamo can be especially important on the nightside, where PPEF and DDEF effects are comparable (Maruyama et al., 2005).

The storm time EF strongly affect the low-latitude ionosphere, by strengthening the equatorial fountain effect on the dayside and in the postsunset region and by causing an overall enhancement of the low-latitude electron density (Astafyeva, 2009a, 2009b; Astafyeva, Zakharenkova, & Doornbos, 2015; Mannucci et al., 2005; Tsurutani et al., 2004). At the magnetic equator, the disturbed EF may alter the direction of the EEJ causing a counter electrojet (CEJ) (Kikuchi et al., 2000; Rastogi, 2006; Yamazaki & Kosch, 2015), and they also may influence the behavior of the ionospheric Es layer, causing development or disruption of the Es layer (Abdu et al., 2013; Rastogi et al., 1971; Singh & Sripathi, 2017).

Besides electric fields, the low-latitude ionosphere may be impacted by the direct effect of thermospheric winds. The neutral winds can raise or lower the *F* region electron density peak height, by pushing ions and electrons up or down along magnetic field lines from high and middle latitudes to low latitudes. As a result, thermospheric winds can drive quite strong positive ionospheric storms at middle and low latitudes (e.g., Goncharenko et al., 2007; Lu et al., 2008; Paznukhov et al., 2009).

During the current 24th solar cycle the sunspot activity has been the lowest in over a century. Consequently, only a few intensive geomagnetic storms with a Dst (World Data Center for Geomagnetism, Kyoto, et al., 2015a) excursion below −100 nT occurred, and only two major events with Dst below −200 nT were recorded during the last 8 years. The largest storm of the 24th solar cycle, the 2015 St. Patrick's Day storm of 17–18 March 2015, has been studied in detail by a variety of instruments (e.g., Astafyeva, Zakharenkova, & Foerster, 2015; Hairston et al., 2016; Huang et al., 2016; Kuai et al., 2016; Ramsingh et al., 2015; Tulasi Ram et al., 2016; Venkatesh et al., 2017; Verkhoglyadova et al., 2016; Zakharenkova et al., 2016). However, the second largest storm of the current solar cycle with the minimum Dst excursion of −207 nT that occurred on 22–23 June 2015, has received much less attention from the scientific community. Astafyeva et al. (2016) performed a preliminary study of the ionospheric response to the geomagnetic storm of 22–23 June 2015. By using measurements of the in situ electron density and the vertical electron content (VTEC) over Swarm satellites, Astafyeva et al. (2016) observed both positive and negative ionospheric storm signatures in the topside ionosphere during the main phase of this storm. Astafyeva et al. (2016) found that the observed ionospheric effects were driven by the PPEF during the beginning of the main phase of the storm, whereas a strong positive effect that occurred during the end of the main phase was difficult to explain. The global overview of ionospheric and thermospheric effects due to the June 2015 storm and due to substorms that preceded the storm, was done by Astafyeva et al. (2017). They showed that the storm provoked significant effects in the thermosphere and ionosphere. In the thermosphere, the storm time enhancement of the neutral mass density on the dayside exceeded the quiet-time levels by 300–500%. In the ionosphere, strong positive storm signatures were observed at the beginning of the storm, led by the strong PPEF effects. At the end of the main phase of the storm, another prominent positive ionospheric storm was observed. It was attributed to a combination of PPEF and thermospheric winds.

The main focus of this work is to analyze the equatorial and low-latitude electrodynamic and ionospheric disturbances during the June 2015 storm. We specifically focus on features in American and Asian sectors, and we discuss explicitly the second positive ionospheric storm that so far has not been resolved. For our study, we use data from ground-based Global Positioning System (GPS) receivers, magnetometers, and ionosondes. In addition to that, we use data from several satellite missions (Swarm, C/NOFS, DMSP, and GUVI). Such set of instruments provides information on ionospheric storm time changes not only at different longitudes and latitudes but also at different altitudes.

2. Results and Discussions

2.1. Geomagnetic Disturbances of 22–23 June 2015

On 22 June 2015, several substorms and a major geomagnetic storm occurred at Earth. These geomagnetic disturbances were caused by two interplanetary shocks (IS) that arrived at ~5:45 UT and at ~18:38 UT (Figure 1). The first IS (IS1) caused an enhancement in the substorm activity, as seen from the auroral electrojet (AE) index (World Data Center for Geomagnetism, Kyoto, et al., 2015b) in Figure 1d. From ~14 UT on 22 June the AE index experienced a second strong enhancement up to ~1.300 nT that lasted until ~17:30 UT (Figure 1d). The effect of this substorm can be seen in the ~ − 40 nT decrease of the SYM-H index (Figure 1c).

The second IS (IS2) was accompanied by a sudden increase in the solar wind speed Vsw from ~450 km/s to ~700 km/s and provoked a major geomagnetic storm. With the beginning of the storm, SYM-H first increased by +77 nT, and from ~19:20 UT started to rapidly decrease and turned negative. The minimum SYM-H value of −207 nT was reached by ~4:30 UT on 23 June 2015 (Figure 1c). During this major storm, the IMF Bz changed polarity several times: it was directed southward at the initial phase of the storm from 18:38 to ~20 UT, with the minimum of −37.6 nT at ~19:20 UT; it then turned northward for ~1.5 h and the maximum of +26.3 nT was reached by 20:30 UT (Figure 1b). From ~20:55 UT to 21:15 UT the IMF Bz was negative again, and from ~21:20 UT it changed to positive and remained there until 00:50 UT of the next day. On 23 June, from ~00:55 UT to ~01:50 UT small-amplitude fluctuations of the IMF Bz can be seen (Figure 1b). From 01:55 UT to 05:30 UT the Bz component was negative, and then positive from ~05:30 UT to 07:30 UT, and the last large-amplitude Bz negative event occurred between ~08:00 UT and ~11:30 UT. Figure 1c shows that the recovery phase started at ~4:30 UT; however, the recovery was rather slow and gradual, as the SYM-H index went slightly down again with the last turn of the Bz to negative values. The interplanetary electric field (IEF) Ey component, depending on the IMF Bz and on the solar wind speed as –Vsw × Bz (http://omniweb.gsfc.nasa.gov), fluctuated between −15 and +20 mV/m during this storm (Figure 1e).

The AE index shows that the auroral and substorm activities were enhanced during this storm (Figure 1d). The maximum of ~2,300 nT was reached at the beginning of the main phase of the storm. The AE further grew during the next long-time southward Bz turnings from ~01:55 UT to 05:30 UT and from ~08:00 UT to 12:00 UT.

Below we discuss electrodynamical and ionospheric disturbances due to the 22–23 June 2015 geomagnetic storm. To better understand the storm time effects, we compare our results with the reference day—(20 June 2015)—that was both in the list of CK days and the first international Quietest Day of that month.

2.2. Disturbances in the Equatorial EEJ: Data From Swarm and Ground-Based Magnetometers

Figures 1f and 1g present temporal variations of the EEJ as derived from Swarm A (SWA) and Swarm B (SWB) magnetic measurements in the ~11 LT and ~13 LT sectors, respectively, during the 2 days of the storm. The spatial position of the SWA and SWB during these measurements can be found in Figure 5.

The EEJ is estimated from scalar magnetic field measurements of the satellites during daytime (06 to 18 LT) satellite passes by subtracting main, crustal, and magnetospheric field models, as well as an Sq spherical harmonic model (Alken et al., 2014; Alken, Maus, et al., 2013; Manoj et al., 2013). The resulting scalar residual corresponds to the magnetic signature of the EEJ. It should be noted that contrary to ground-based data, in satellite observations the negative EEJ magnetic field signatures indicate eastward current flow, while the positive signatures are for westward EEJ, that is, for the CEJ.

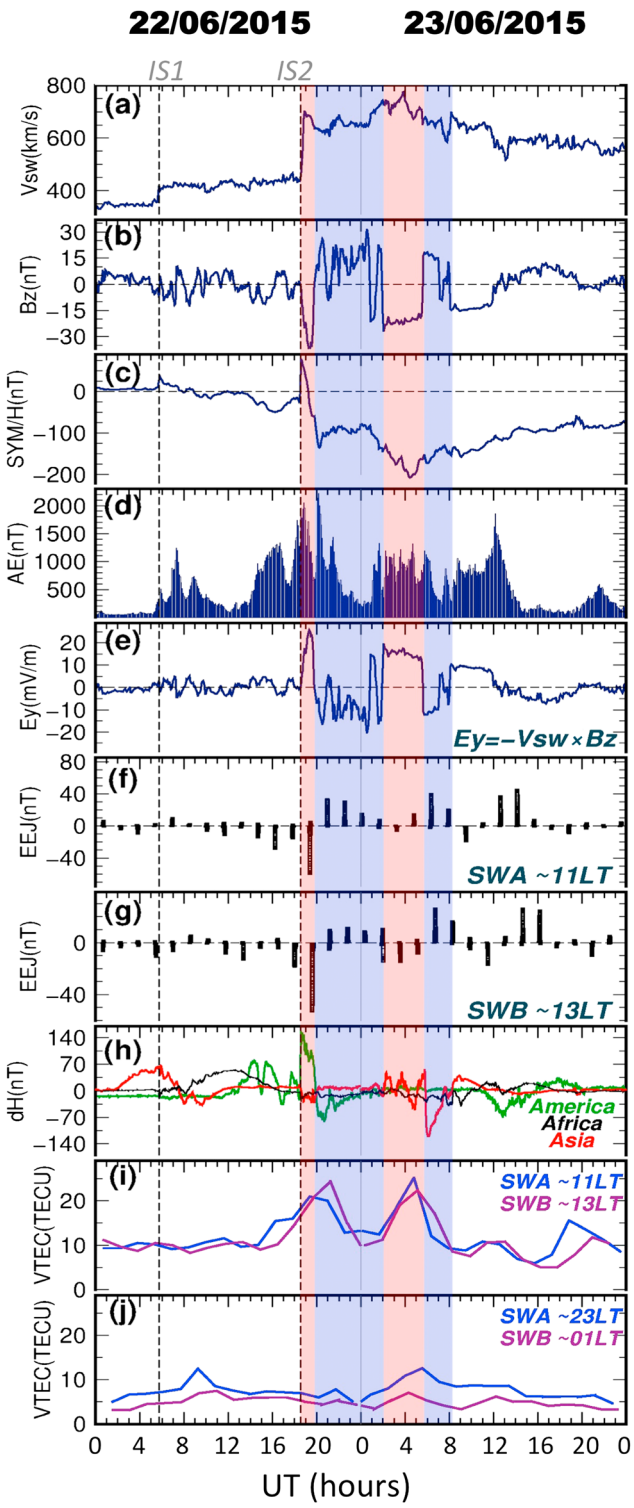

Figure 1. Interplanetary, geomagnetic and ionospheric conditions during the days of the geomagnetic storm of 22–23 June 2015. (a) Solar wind speed Vsw, (b) interplanetary magnetic field (IMF) Bz, (c) SYM-H index, (d) AE index, (e) IEF Ey; (f, g) equatorial electrojet (EEJ) as retrieved from magnetic measurements onboard Swarm A (SWA) at ~460 km altitude and Swarm B (SWB) at ~530 km altitude, respectively, (h) dH from ground-based magnetometers in the American (green, LT = UT − 4.6 h), African (black, LT = UT − 1 h), and Asian (red, LT = UT + 7 h) longitudinal sectors. The dH is estimated from the following pairs of magnetometers: *puer-leti* (American), *sam-mbo* (African), *pukt-bang* (Asian); (i, j) low-latitude vertical total electron content (VTEC) measured by SWA and SWB during the dayside passes (i) and night-side passes (j). The VTEC is averaged over ±30° of geographical latitude. The vertical dotted lines and labels *IS1* and *IS2* on the top denote the two interplanetary shocks that arrived on 22 June at 6:45 UT and at 18:38 UT. Thin vertical gray line delimits the 2 days, 22 and 23 June. The red- and blue-shaded rectangles define the periods of negative and positive IMF Bz, respectively, during the main phase of the storm.

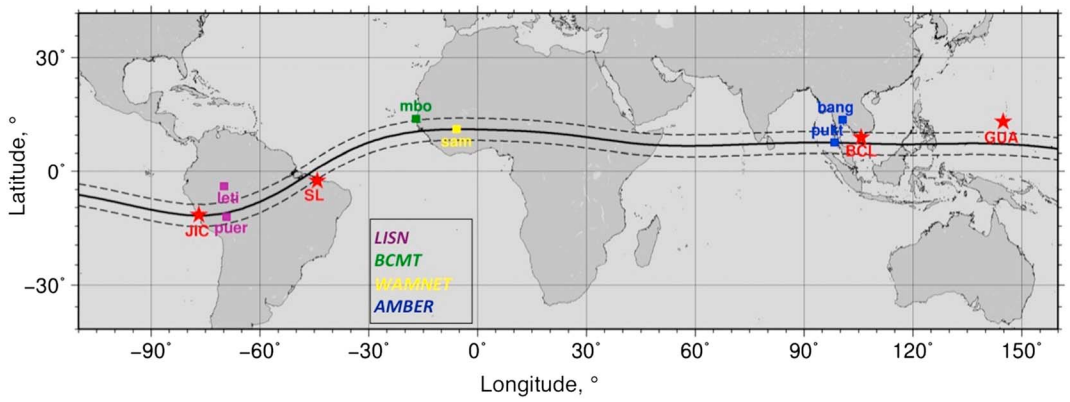

Figure 2. Geographical location of ground-based instruments (magnetometers and ionosondes) used in this study. Black thick curve denotes the position of the magnetic dip equator, thin dotted lines along the dip-equator show ±3° range where the equatorial electrojet can be observed. The names of both magnetometers (colored squares) and ionosondes (red stars) are shown next to them. Color codes for magnetometers identify the operating networks, as shown.

Figures 1f and 1g show that the EEJ behavior in 11 LT (SWA) and 13 LT (SWB) sectors was similar but not one-to-one identical, especially outside the period of the geomagnetic storm. Such a difference might be, first of all, due to the fact that SWA is about 70 km lower in altitude than SWB, so it will generally see a larger magnetic field signature from the EEJ. Second of all, the difference can be explained by rapid changes in the current system.

On 22 June 2015, the first small-amplitude changes in the EEJ occurred from ~14 UT to 16 UT, when the EEJ at SWA was eastward during ~4.5 h and reached −35 nT at ~16 UT (Figure 1f). At SWB, the EEJ reached the minimum of −20 nT at 18 UT (Figure 1g). The observed EEJ enhancements were, most likely, due to the enhancement of substorm activity from ~14 UT to ~18 UT (Figure 1d).

With the beginning of the storm at 18:38 UT on 22 June, the EEJ in both local sectors significantly intensified: in the ~11 LT sector, the EEJ decreased to −70 nT, while in the ~13 LT sector it reached −55 nT (Figures 1f and 1g, respectively). These Swarm EEJ results show occurrence of the eastward EEJ which agrees with the IEF Ey behavior (Figure 1e). From ~19:45 UT, the IEF Ey changed the polarity, and the next satellite passes showed the EEJ sign change along with the decrease in the electrojet intensity. The CEJ signatures remained present during the next Swarm passes, and by ~2 UT on 23 June the CEJ further decreased.

From 2 to 6 UT, the IEF Ey was steadily positive, but SWA and SWB showed different results. At SWB, the EEJ was negative of −15 nT, that is, corresponded to the eastward IEF Ey direction, while at SWA the EEJ changed from positive to negative and was less intense. The SWA observations, most likely, indicate rapid changes in the equatorial electric fields during this period of time. From ~6 UT the IEF Ey turned negative/westward, and another CEJ event was registered by both Swarm satellites. This CEJ seemed to last for ~4 h. One more CEJ event was observed at the recovery phase of the storm from ~12 UT to ~16 UT on 23 June 2015. These observations lead us to conclude that at the beginning of the storm, that is, from 18:38 UT on 22 June to ~2 UT on 23 June, the equatorial zonal electric fields were largely impacted by the PPEF effect. Then, from ~2 UT on 23 June, the EEJ changed to CEJ several times, which is, most likely, due to the DDEF that was developed at this stage of the storm.

In addition to the space-based EEJ data, we investigate measurements from ground-based magnetometers at equatorial latitudes in American, African, and Asian regions (Figure 2). The EEJ can be estimated by using a pair of magnetometers, located—one at the dip equator and the other at ~6–9° of magnetic latitude away from it (Anderson et al., 2002, 2006; Rastogi, 1989; Yizengaw et al., 2012, 2014). First, we remove the nighttime baseline from the H measurements of all magnetometers in order to avoid different offsets in their data. Second, we obtain the EEJ signature by taking the difference between the H component measurements performed by a pair of at-the-equator and off-the-equator magnetometers. It is known that the magnetometers manifest the response to the Sq currents and to the ring current. In addition to that, magnetometers located within ±3° of latitude from the magnetic dip equator show strong enhancement in the H-component because of the EEJ, while magnetometers located at 6°–9° of latitude would have zero-response to the EEJ. Consequently, the difference between the measurements by a pair of dip-non-dip magnetometers (dH)

Table 1
Information on Magnetometer (M) and Ionosonde (I) Stations Used in This Work

I/M	Station code	Location (GLon;GLat)	LT	Location (country)	Network/Source
M	Leti	−69.94; −4.19	UT − 4.6 h	Leticia (Brasil)	LISN[a]
M	Puer	−69.19; −12.58	UT − 4.6 h	Puerto Maldonado (Peru)	LISN[a]
M	Mbo	−16.9; +14.39	UT − 1.1 h	Mbour (Senegal)	BCMT
M	Sam	−5.62; +11.39	UT − 0.3 h	Samogossoni (Mali)	WAMNET[b]
M	Bang	+100.6; +14.08	UT + 6.7 h	Bangkok (Thailand)	AMBER[c]
M	Pukt	+98.35; +7.89	UT + 6.6 h	Phuket (Thailand)	AMBER[c]
I	JIC	−76.8; −12.0	UT − 5.1 h	Jicamarca (Peru)	GIRO[d]
I	SL	−44.2; −2.6	UT − 2.9 h	Sao Luis (Brazil)	GIRO[d]
I	BCL	+105.71; +9.3	UT + 7 h	Bac Lieu (Vietnam)	SEALION
I	GUA	+144.86; +13.62	UT + 9.6 h	Guam (Guam)	GIRO[d]

[a]– Valladares and Chau (2012). [b]– Alken, Chulliat, et al. (2013). [c]- Yizengaw and Moldwin (2009). [d]– Reinisch and Galkin (2011).

would give the EEJ signature and would remove other responses. We apply this method for three pairs of magnetometers as shown in Figure 2 and in Table 1.

Our results of the dH estimated in American, African, and Asian regions are shown in Figure 1h. One can see that the behavior and the intensity of the dH is different in these three regions, depending on the local time in each sector: LT = UT − 4.6 h for the American, LT = UT − 1 h for the African and LT = UT + 7 h for the Asian sector. Quiet-time dH variations normally show a steady increase starting at ~7–8 LT with maximum at ~12–13 LT, and then steady decrease until ~18–19 LT (Figures 3a and 3d, dotted curve).

Figure 1h shows that on 22–23 June 2015 the strongest storm time effects occurred in the American region when it was in local daytime hours. The first deviation from the diurnal dH pattern was observed

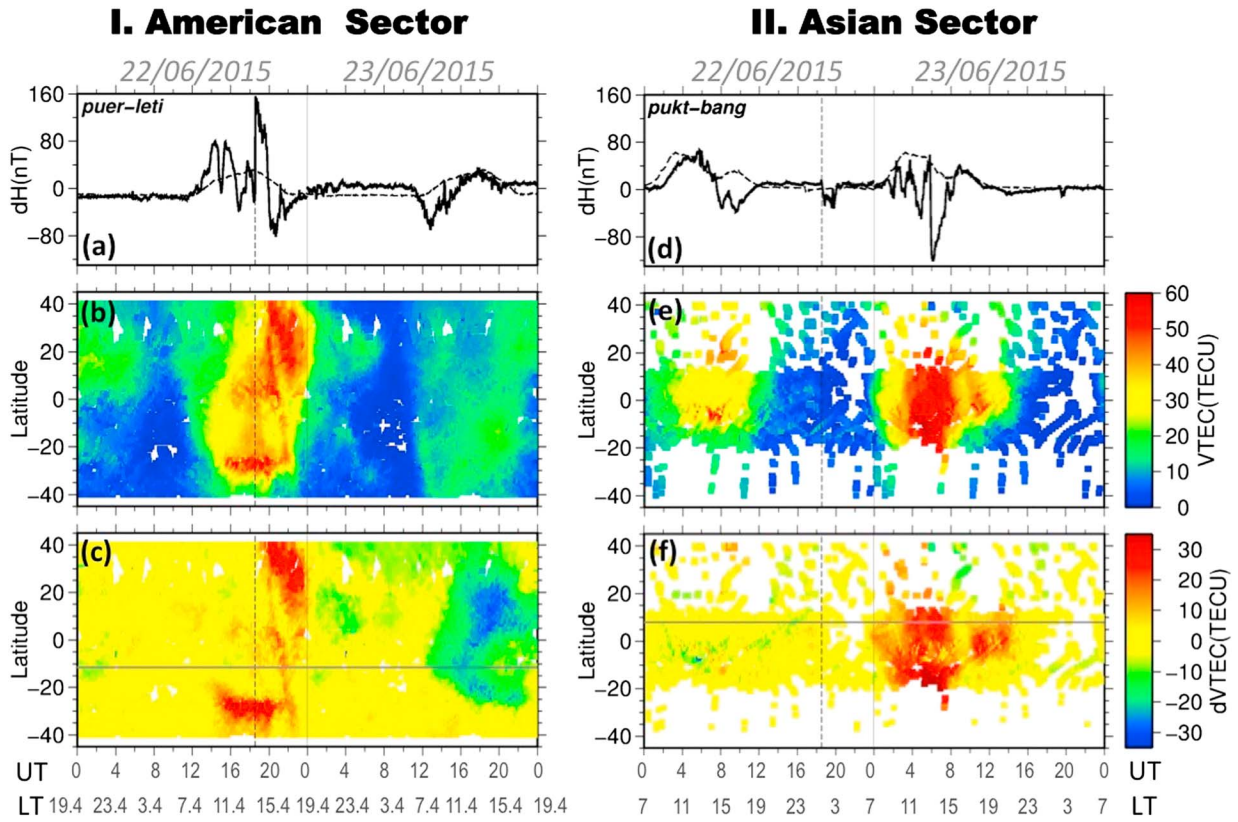

Figure 3. (a, d) Variations of the horizontal intensity of the geomagnetic field (dH) in the American and Asian sectors, respectively, for the 2 days of the storm; (b, e) VTEC and (c, f) storm-to-quiet residual dVTEC at the longitudes of the magnetometers (−70° and 100°E, respectively). The UT and LT scales are shown on the bottom. On panels (b)–(f) horizontal gray lines indicate the position of the magnetic dip equator.

at 13–15 UT, when the dH increased to +80 nT. At ~15 UT, the dH suddenly decreased to zero level. It further went up to +80 nT, and from ~15:30 UT, a second longer-time dH decrease occurred. From ~17:30 UT the dH turned positive up to 50 nT. We suggest such dH changes can be due to the enhanced substorm activity (Figure 1d). With the storm commencement at 18:38 UT, we observed a sudden increase in dH of ~140 nT. This dH enhancement lasted until ~19:45 UT, which is consistent with fluctuations of IEF Ey (Figure 1e). From 19:45 UT to ~22 UT one can see negative dH which signifies the occurrence of the CEJ with magnitude of −70 nT. These fluctuations are in line with the EEJ observations from Swarm (Figures 1f and 1g). On 23 June and at the recovery phase of the geomagnetic storm, we observed another significant deviation of the dH behavior from the diurnal pattern, as at ~11 UT (i.e., at ~6.4 LT) the dH decreased and intensified, which is contrary to the daytime behavior of the dH. This decrease in the dH lasted until 14 UT and, most likely, related to DDEF as often observed during the recovery phase periods (e.g., Kikuchi et al., 2000).

The dH behavior in the Asian region (red curve in Figure 1h) was also impacted by substorms and the storm that occurred on 22–23 June 2015. The daytime dH first fluctuated during the arrival of the IS1 at 05:45 UT on 22 June, causing only ±10 nT fluctuations. At ~7.3 UT (i.e., ~13.8 LT), the dH turned negative, which signifies occurrence of the CEJ, and remained that for about 2 h. From 8.8 UT the CEJ slightly intensified again. The storm commencement can be seen as small amplitude dH decrease of −20–30 nT from 18.5 to 20 UT. The strongest storm time alterations in the Asian sector can be seen on 23 June, when the normal daytime steady increase was "replaced" by several short-term intensive fluctuations from positive to negative dH values, which implies several fast changes between the EEJ and CEJ from 2 to 8 UT (i.e., from 9 to 15 LT). It is interesting to note that from ~2 to ~5.6 UT the IEF Ey was steadily eastward, while dH changed 3 times from eastward to westward and back, which is in line with our previous conclusion on the DDEF competing with the PPEF at this time. We note that these ground-based observations are in agreement with the EEJ data from both Swarm satellite measurements that were made over the Asian region as well (Figures 1f and 1g). From ~5.6 UT, the IEF Ey turned westward and caused the most intensive and sudden EEJ change to CEJ that lasted until ~8 UT. The minimum of the dH of −110 nT was observed at ~6.1 UT on 23 June. This CEJ was, most likely, intensified by the DDEF. It is interesting to note that dH measured by magnetometers in Indian sector (i.e., ~30° westward from our observations), show quite similar variations (Singh & Sripathi, 2017).

In the African sector (Figure 1h, black curve), the disturbance alterations were much smaller than that in the American and Asian sectors. The daytime dH behavior was slightly impacted by substorm activity enhancement at ~5–9 UT on 22 June 2015. When the geomagnetic storm commenced at 18:38 UT, in the Asian sector (which was the local evening time), the EEJ experienced a small decrease during the first 1.5 h of the storm. On 23 June 2015, the diurnal pattern of the EEJ was perturbed by the storm time EF, so that we did not observe the normal daily enhancement from ~8 UT, as the day before. Instead, a small decrease occurred from ~4 UT and lasted until ~10 UT.

Below we discuss low-latitude ionospheric storm time effects in the American and Asian regions.

2.3. Low-Latitude Ionospheric Effects in American and Asian Sectors

As we concluded above, the EF during the first part of the June 2015 storm was driven by the PPEF, whereas at the second part of the storm the PPEF seemed to compete with the DDEF. It is of interest to investigate the effects in the low-latitude ionosphere during these periods of time. Figures 1i and 1j shows low-latitude ionospheric VTEC estimated from GPS receivers on board SWA and SWB spacecrafts during the day and night parts of the orbits, respectively. Note that these curves represent the topside part of the VTEC, that is, above ~460 km (SWA) and ~530 km (SWB) of altitude. One can see the occurrence of two positive storms. First, with the beginning of the storm, the dayside VTEC increased at both satellites (Figure 1i). The VTEC started to decrease shortly after the IMF Bz turned northward, and by ~24 UT the VTEC returned to quiet-time values of ~10 TECU at both satellites. The second strong increase of the low-latitude VTEC was observed from ~2 UT on 23 June, when the IMF Bz turned negative again, but both Swarm and ground-based dH measurements showed rapid fluctuations of the EEJ. The latter makes it doubt that PPEF or DDEF were the main drivers for this major second positive ionospheric storm. On the nightside, no effect was observed during the first part of the storm. However, from ~2 UT, one can see a small VTEC increase on both satellites, that lasted until ~5.6 UT, when the IMF Bz turned northward.

It should be noted that the first positive ionospheric storm was captured by Swarm over the American sector, while the second one—over the Pacific and Asian sector. It is therefore of interest to analyze in more details the ionospheric behavior in these two regions by using local instruments. The GPS VTEC with 5 min resolution are available from the Massachusetts Institute of Technology Haystack Observatory Madrigal database (Rideout & Coster, 2006). Figure 3 shows variations of the dH and the VTEC derived from ground-based GPS receivers calculated at low latitudes along the longitudes of the magnetometers (70°W and 100°E, for the American and Asian sectors, respectively) for the 2 days of the storm. To better understand the storm time VTEC alterations (dVTEC), we remove the quiet-time reference values of 20 June 2015 from the storm time values. One can see that in the American sector, the first deviation from the quiet-time values was observed in the Southern Hemisphere from ~14 UT on 22 June 2015. With the development of the geomagnetic storm, we observe a strong increase of the low-latitude VTEC, especially in the Northern Hemisphere. From 01 UT to 05 UT on 23 June, the low-latitude VTEC in the Northern Hemisphere went by ~10–15 TECU below the quiet-time value, and much stronger negative storm was observed during the recovery phase from ~12 to ~23 UT (Figures 3b and 3c).

In the Asian sector, at the beginning of the storm the VTEC did not show significant storm time changes at low latitudes (Figures 3e–3f). The most interesting feature is observed from 2 to 8 UT (from 9 to 15 LT) on 23 June, when the dH first fluctuated between positive and negative, and then turned largely negative, but the low-latitude dVTEC showed a very prominent increase of +30 TECU. Note that this positive dVTEC effect is asymmetric with regard to the magnetic dip equator (Figure 3f), which might indicate on the role of thermospheric winds in this ionospheric enhancement. Indeed, the storm occurred during the June solstice, when the background thermospheric circulation is directed from summer to winter, that is, from NH to SH. The storm time circulation is directed equatorward and superimposed on the background circulation. Consequently, in the NH (summer) the winds are stronger, and perturbations can be easily transported to middle and low latitudes than in the SH (winter). Also, we note that we do not observe clear signatures of superfountain effect at low latitudes, and no depletion can be seen over the magnetic equator.

Further, we analyze data from ionosondes located in the American and Asian sectors (Figure 2 and Table 1). The ionosondes make it possible to investigate the electron density and the ionospheric height changes. Besides these main parameters, modern ionosondes can measure ionospheric drifts, as they operate as High Frequency Doppler radar systems (Reinisch et al., 1998). We note that in our work HmF2 was deduced from manually edited ionograms by using the SAO-Explorer software.

Figure 4 shows variations of electrodynamical and ionospheric parameters in the American (column I, left) and Asian (column II, right) sectors during a 24 h period from 10 UT on 22 June 2015 to 10 UT on 23 June 2015. To better understand the interplanetary and auroral impact on the ionosphere and electrodynamics, we compare these parameters with the variations of the IMF Bz components (h1, h2) as well as with the AE index (i1, i2). It should be noted that Jicamarca (JIC), Sao Luis (SL), and Bac Lieu (BCL) ionosonde stations are located very close to the magnetic equator, while Guam (GUA) is situated several degrees outside the EEJ area (Figure 2). In longitudes, the American and Asian instruments are separated by ~12–13 h in time, which allows us to simultaneously analyze the storm time effects on the opposite sides of the globe.

As mentioned above, in the American sector, some effects occurred before the storm and were most likely due to substorms. Figure 4 shows that from ~13 UT to 16:30 UT Jicamarca ionosonde, located ~7° of longitude on the west from the magnetometers, showed that the critical frequency foF2 decreased as compared to the quiet-time curve (Figure 4e1). The HmF2 first increased to ~400 km and then decreased to 250 km by ~15 UT. By ~16 UT, the HmF2 increased again to ~450 km, and during this last increase we observe the occurrence of the ionospheric F3 layer (Figure 4f1). At Sao Luis ionosonde station, located ~26° of longitude on the east from Jicamarca, no noticeable changes were observed before the storm commencement, except for a small foF2 increase ~1–1.5 h before the storm (Figures 4e1–4g1), which is similar to JIC observations.

At the beginning of the geomagnetic storm at 18:38 UT, the Jicamarca ionosonde and the magnetometers were in the early afternoon hours, and the EEJ showed sudden intensification up to +150 nT immediately at the storm commencement and changed sign at 19.45 UT following the IEF Ey behavior (Figure 4b1). Unfortunately, no plasma drift (Vz) data were available from the Jicamarca ionosonde during the beginning of the storm. From ~19.5 UT to ~20.5 UT, we observed small-amplitude fluctuations of the Vz within ±25–30 m/s. The most significant drifts over Jicamarca were observed between ~1 UT and ~5 UT (~21.4 LT

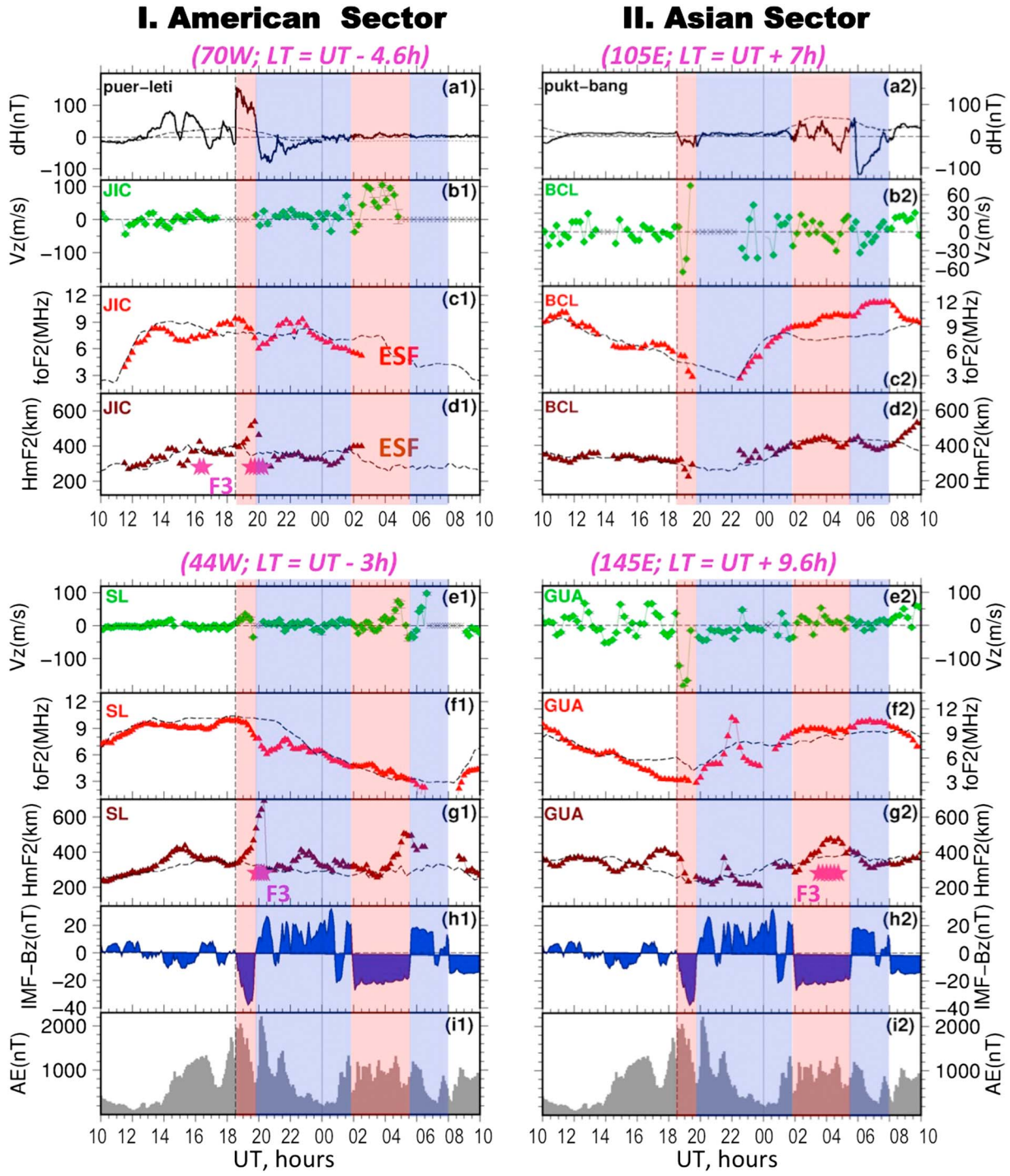

Figure 4. Variations of the magnetic, electrodynamic and ionospheric parameters from 10 UT on 22 June 2015 to 10 UT on 23 June 2015 in the American region (left) and Asian region (right): (a1, a2) Variations of the horizontal magnetic field intensity (dH) in the American and Asian regions, respectively, for the disturbed period (thick black curve) and the quiet-time period (thin dotted line). (b1, b2) Green diamonds show the vertical ionospheric drift above the Jicamarca ionosonde (JIC) and Bac Lieu ionosonde (BCL), the error bars are shown in black thin bar lines; (c1, c2) ionospheric critical frequency foF2 during the disturbed period (red triangles) compared with the quiet-time levels (gray dashed curve) at JIC and BCL; (d1, d2) ionospheric maximum height HmF2 (brown triangles) and the reference values (gray dashed line) at JIC and BCL. Labels "ESF" and "F3" indicate the occurrence of the equatorial spread *F* (ESF) and *F*3 layer on the ionograms (examples are shown in Figures S1 and S2 in the supporting information); (e1, e2) vertical drift over SaoLuis (SL) and Guam (GUA) ionosondes; (f1, f2) variations of foF2 recorded by SL and GUA, respectively; (g1, g2) variations of HmF2 over SL and GUA; (h1, h2) the interplanetary magnetic field (IMF) Bz component; (i1, i2) AE index; The red- and blue-shaded rectangles delimit the periods of negative and positive IMF Bz, respectively, during the main phase of the storm, as in Figure 1. The reference values taken are those for 20 June 2015. Dashed vertical lines indicate the storm commencement. Thin gray vertical line denotes the 00 UT line. Ionosonde data have the following time resolution: JIC = 15 min, SL = 10 min, BCL = 10 min, and GUA = 15 min.

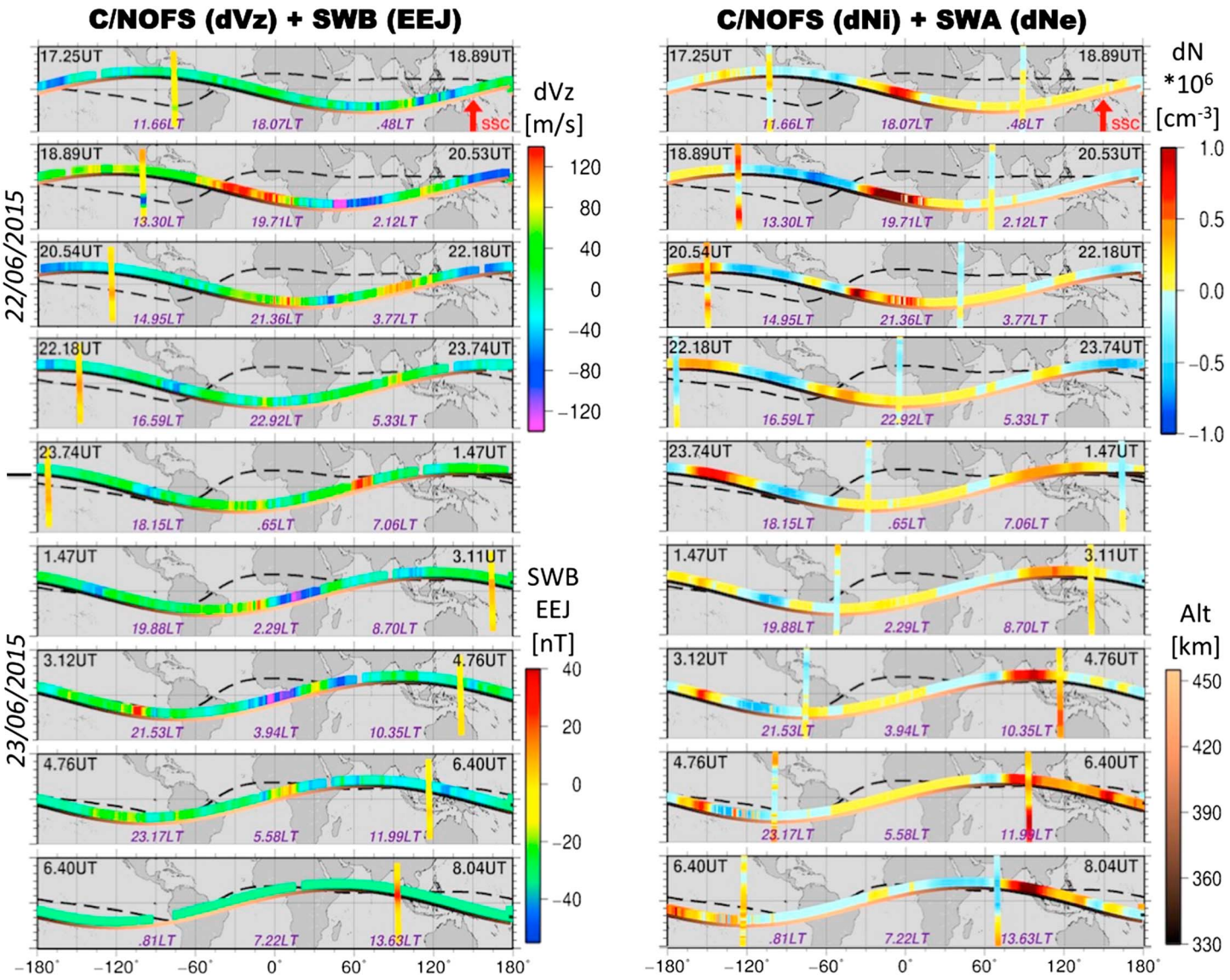

Figure 5. Results from C/NOFS and Swarm results during the main phase of the 22–23 June 2015 as compared to quiet-time values measured on 19–20 June 2015. (left) Deviations of the vertical plasma drift (dVz) and SWB EEJ measurements in the 13 LT sector (vertical red-to-blue colored lines). The corresponding color scales are shown on the right of the panel. (right) The differential ion density (dNi) measured by C/NOFS and the electron density (dNe) as measured by Swarm A satellite at the altitude of ~460 km in the ~11 LT sector. The dNi/dNe color scale is shown in the right upper corner. In all panels, thin black-brown curves along the C/NOFS measurements denote the changes of the spacecraft orbital altitude, the corresponding color scale is shown in the right bottom corner of the figure. Each panel shows the UT of the beginning and the end of the corresponding C/NOFS track. The local time (LT) of the C/NOFS satellite track is shown in purple italic. It should be noted that the UT indicated on the panels corresponds to C/NOFS satellite pass, and only approximately to Swarm. The exact UT of the Swarm A and B equatorial measurements can be found in Figure 1f. The range of latitudes for all panels is ±30°. Dashed black curve shows the magnetic dip equator, red arrows on the top panels indicate the SSC time.

to 0.4 LT) on 23 June, when the upward drift increased up to 120 m/s (Figure 4b1). This enhanced upward drift event corresponds to fluctuations of the IMF from northward at 1 UT to southward turn at ~2 UT. Note that Vz is constantly upward from ~2.75 UT to 5 UT, while the IMF Bz is southward throughout this period of time. The ionospheric critical frequency foF2 equaled to ~10 MHz at the storm commencement, but started to decrease with the development of the storm and reached the minimum value of ~6 MHz by 19:45 UT. The maximum ionospheric height HmF2 started to rapidly increase at the storm commencement and reached 575 km by ~19:45 UT (Figures 4c1 and 4d1). During this rapid increase in the HmF2, we observed the occurrence of the ionospheric *F*3 layer (some examples of ionograms can be found in Figures S1 and S2 that are available as supporting information). The *F*3 layer is a "temporary additional" layer in the ionosphere that

often occurs in result of the storm time-enhanced equatorial upward E × B drift and rapid ionospheric uplift due to eastward penetration electric fields (e.g., Lin et al., 2009; Paznukhov et al., 2007; Zhao et al., 2005). From 19:45 UT, the IMF Bz changed the polarity from negative to positive, and consequently, the EEJ changed from eastward to westward, which led to increase of the foF2 and sudden decrease of the HmF2. From ~3 UT to 11 UT on 23 June strong equatorial spread *F* (ESF) effect was observed in JIC data (Figure S1).

The Sao Luis ionosonde showed similar response to the storm commencement, but the effect of the sudden ionospheric uplift was much stronger, as the HmF2 rose to 700 km (Figures 4f1–4g1), accompanied by the occurrence of the *F*3 layer (Figure S1). With the second long-term southward turn of the IMF Bz, starting from 2 UT (i.e., from 23 LT), foF2 steadily decreased at SL station. However, HmF2 increased from ~250 to 500 km at 3.5–5.5 UT (0.5–2.5 LT), and the vertical drift over SL station increased up to 90 m/s (Figure 4e1), which is contrary to the PPEF effects on the nightside, but in line with DDEF effect.

In the Asian sector, the beginning of the storm fell onto local night hours. At the storm commencement, the vertical plasma drift Vz at BCL first went sharply downward (−70 m/s), but at ~19:30 UT it changed the direction to upward and reached +80 m/s (Figure 4b2). It may be noted that during this period of time in the Indian sector the *F* layer was also in downward motion (Singh & Sripathi, 2017). The critical frequency foF2 and the ionospheric height HmF2 decreased ~30 min after the storm commencement. The minimum value of the foF2 of ~3 MHz was measured at 19:45 UT, and HmF2 descended to ~220 km at 19:30 UT, and went back to 320 km at 19:45 UT. Unfortunately, no measurements were done between ~19:45 UT and ~22:15 UT (Figures 4c2–4d2).

From 22:15 UT, foF2 started to increase, and from 2 to 9.5 UT it largely exceeded the quiet-time foF2 curve, reaching ~12 MHz by ~8 UT. During this period of time, the IMF Bz persisted to be negative but the dH showed several fluctuations within ±45–50 nT, and from 5.6 UT dH went down to −120 nT. Figure 3b2 shows that the vertical plasma drift variations somewhat followed the dH behavior, as we observe similar polarity changes in the Vz data at BCL. The HmF2 parameter remained close to the quiet-time reference value from 2 to 7 UT and increased after 8 UT (Figure 3d2). It should be noted that BCL is located very close to the magnetic equator, and the observed gradual but significant enhancement of the electron concentration over BCL does not seem related to or driven by the equatorial electrodynamic effects.

At Guam station (~40° eastward from BCL), the downward plasma drift at the beginning of the storm was much stronger than at BCL. The Vz varied within ±60–80 m/s before the storm, and with the storm commencement it reached −180 m/s (Figure 4e2). This strong effect lasted until 19:45 UT, that is, until the IMF Bz turned positive. The Vz variations were much less pronounced during the rest of the storm. The foF2 parameter was below the quiet-time curve when the storm began, and it only started to increase after 20 UT (Figure 4f2). By ~22:30 UT a sudden strong increase of the foF2 up to 11 MHz was observed at GUA station. The foF2 further went down below the quiet-time reference curve, and from ~01:30 UT it increased again. This latter increase was accompanied by HmF2 increase and *F*3 layer effect (Figures 4f2–4g2 and Figure S2).

In summary, the ionosonde results in both sectors are in line with our previous conclusions on main drivers acting at the beginning and at the end of the main phase of the storm.

2.4. Variations of Ion Density and Vertical Ion Drifts as Seen by C/NOFS Satellite

The Communications/Navigation Outage Forecasting System (C/NOFS) satellite was launched in April 2008 and reentered in November 2015; it had the primary scientific objective to study the equatorial ionosphere and, in particular, occurrence of the equatorial plasma bubbles (de La Beaujardiere et al., 2009). It was initially launched into a near-equatorial orbit (inclination 13°) with an initial apogee of 850 km and perigee of 400 km. By June 2015 the apogee and perigee had changed to ~460 and ~330 km, respectively (thin black to brown curve in Figures 5 and 6). Among other instruments, C/NOFS carried the Coupled Ion Neutral Dynamics Investigation (CINDI), thermal plasma instrument containing a retarding potential analyzer and an ion drift meter that provided the information on the ion density, ion drift velocity, total ion concentration, the major ion composition, and the ion temperature. In this work, we analyze data of the ion density Ni and that of the plasma drifts from the ion drift meter instrument onboard C/NOFS. It should be noted that in the Vz data the ion motion in the equatorial region is close to vertical and perpendicular to the local magnetic field line (Hairston et al., 2013). The CINDI instruments originally measure the ion flow in the spacecraft

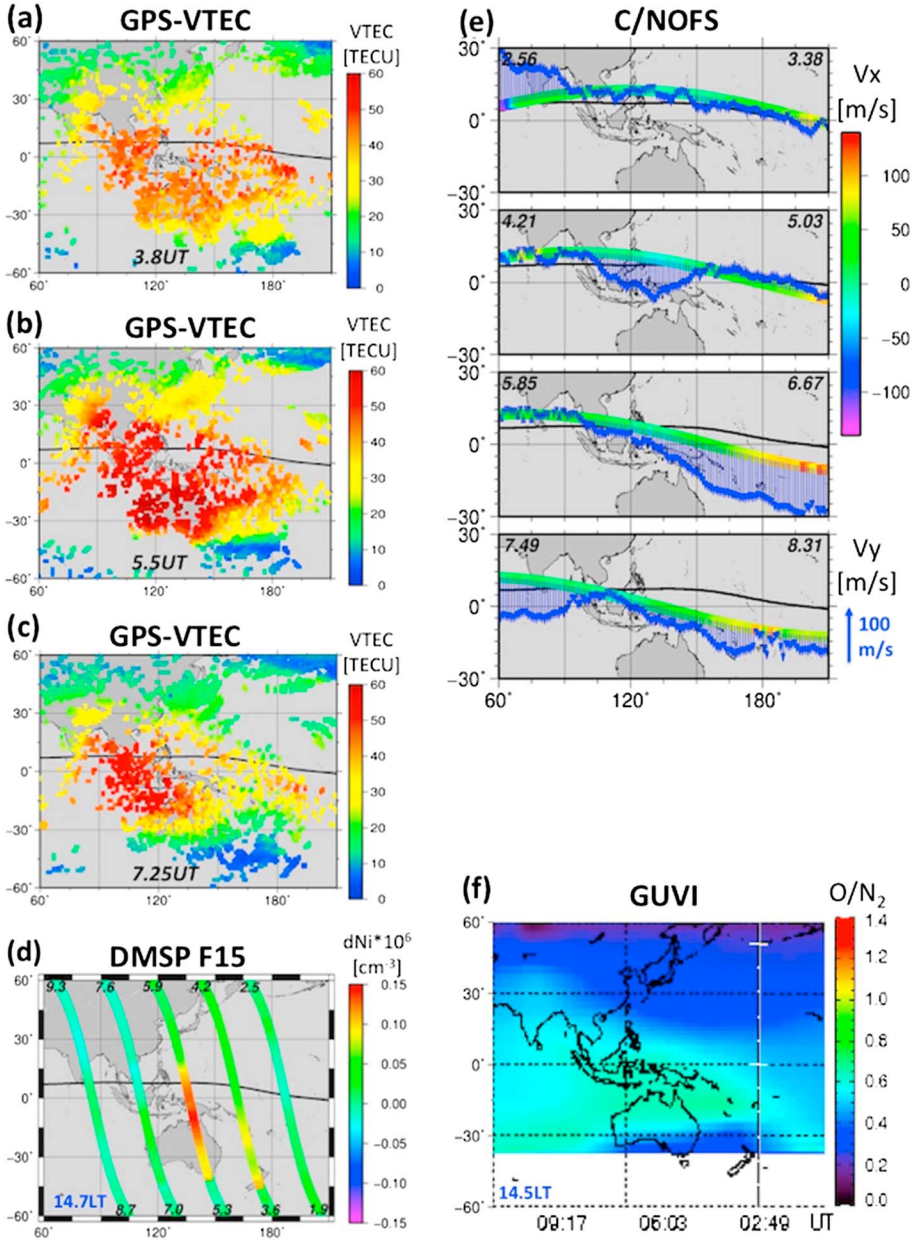

Figure 6. Zoom on the ionospheric and thermospheric effects in Asian sector during the period of time from ~2 to ~11 UT on 23 June 2015. (a–c) GPS-derived VTEC during the positive storm over the Asian region. The UT for each map is shown on the panel; (d) storm time changes in the ion density as compared to the quiet day (20 June 2015) measured by the DMSP F15 satellite at the altitude of ~840–855 km. The passes are ascending and cross the equator at 14.7 LT. Numbers in italic show the time of the passes; (e) the absolute values of the ion flows as measured by C/NOFS spacecraft at the altitude of 350–400 km. Vx (velocity in the direction of the spacecraft) is shown in color and the corresponding color scale is shown on the right. Vy (roughly northward) direction is shown in blue arrows. The black curve shows the magnetic dip equator; (f) thermospheric O/N2 ratio as measured by GUVI satellite at the altitude ~625 km. The UT and LT time of the equatorial crossings are shown at the bottom of the panel.

components, and 3-D velocity vector is transformed into the local magnetic field coordinates (parallel, horizontal perpendicular, and meridional perpendicular).

To estimate the disturbance-induced alterations of the Ni and Vz, we removed the quiet-time levels (measured on 20 June 2015) from the disturbed ones (measured on 22–23 June 2015). Figure 5 (left) shows dVz variations (from C/NOFS) and SWB EEJ measurements in the 11 LT sector. The top left panel shows that

before the storm commencement the residual dVz varied within ±30–40 m/s. With the development of the geomagnetic storm, on the dayside, the dVz increased up to 50–80 m/s. In the evening and postsunset sectors, we observe a strong dVz enhancement of 140 m/s from ~19.5 UT to ~19.8 UT (over the Atlantic Ocean). This result is in agreement with variations of the IMF Bz, that was largely negative from ~18.5 UT to ~19.75 UT and is also consistent with SWA and SWB observations of the strong eastward EEJ on the dayside. From ~19.85 UT to ~20.03 UT, when the C/NOFS flew through the nightside, it registered the deviation of the dVz of about −140 m/s over Eastern Africa and the Indian Ocean. Such dVz behavior is in line with the positive IEF Ey values and also with the Swarm EEJ data at the beginning of the storm, implying plasma upward drift on the dayside and downward drift on the nightside. Figure 1 shows that the IEF Ey changed sign at ~19.75 UT, and consequently, from ~20.0 UT we see the dVz changing sign from positive to negative, and from ~20.4 UT to 20.53 UT we observe negative variations of the dVz in the morning sector.

During the next C/NOFS satellite pass from 20.54 UT to 22.18 UT, SWB measurements showed CEJ signatures and the dayside low-latitude drifts from C/NOFS seem to be negative down to −50 m/s, positive (~ +50 m/s) in the postsunset and nightside sectors, and reach +120 m/s in the early morning sector (~3.77 LT). As the previous pass, the C/NOFS measurements are in agreement with the IMF Bz behavior and with the SWB EEJ estimations. Similar results, but smaller Vz values were observed during the next two C/NOFS passes from 22.18 UT to 23.74 UT and from 23.8 UT to 1.47 UT (Figure 5, first two right panels from the top).

From 1.47 UT to 3.11 UT and from 3.12 to 4.76 UT C/NOFS data detected strong downward storm time drift deviation of −140 m/s in the early night local time sectors, when the satellite was flying over the Africa and the Atlantic ocean. Figure 1 shows that during this period of time, the IMF Bz was southward, which implies penetration of eastward electric field on the dayside and of westward EF on the nightside. The latter might explain the strong downward ion drift in the CNOFS observations during the local night hours.

The next C/NOFS pass from ~4.76 UT to 6.40 UT showed that the previously observed strong downward drift over the Atlantic region switched to upward (+80 m/s). The Vz on the dayside varied within ±40 m/s, while on the nightside it was positive in the range +40 to +80 m/s. During this period of time, the IMF Bz was first negative, but turned positive from ~5.6 UT and both SWA and SWB registered the CEJ occurrence (Figure 1). We note that we do not observe any significant and persistent upward/downward plasma motion over the Asian region where we observed the strong VTEC enhancement. From 6.40 UT to 8.04 UT, the dVz deviated at all longitudes within ±30 m/s, which is close to the prestorm values.

Deviations of the ion density (dNi) from C/NOFS Ni measurements are shown in Figure 5 (right column). Note that the apogee altitude of C/NOFS is close to the orbital altitude of Swarm A satellite, so that it is of interest to compare the dNi CNOFS observations with SWA dNe results. Figure 5 demonstrates that on both dayside and nightside, dNe variations from SWA are very similar to dNi variations from C/NOFS.

With the development of the geomagnetic storm, we observe $+1.0 \times 10^{-6}$ cm^3 deviation over the Atlantic Ocean. At this location and at this time we observed the strong upward plasma drift (left column of panels). From 20.54 UT to 22.18 UT, when the IMF Bz turned northward, one can see a strong negative storm on the dayside (over the Pacific Ocean), and positive storm effects in the morning sector (over a part of the Pacific Ocean) and in the evening and postsunset sectors (over Atlantic Ocean). From 22.18 UT to 23.74 UT, and from 22.74 UT to 1.47 UT several small storm time enhancements were observed over central Pacific region, over South America, and over the Asian region. At ~3 UT we observe small dNi and dNe increases over the Asian region. The dNi enhancement over Asia can be seen during the next C/NOFS pass. The next C/NOFS pass, from 4.76 UT to 6.40 UT, showed that this positive effect further extended over the whole Asian and partly Pacific region. During this period of time, SWA dayside observations also showed significant positive storm effects in the Asian region, especially in the SH. From ~8 UT the positive storm over Asian sector started to lessen.

In conclusion, the C/NOFS data are in agreement with the above results from ground-based instruments. We do not observe strong upward/downward motion of the plasma, but the plasma density increases in the Asian region at the end of the main phase of the storm. These interesting results require a specific focus by using other available instruments.

2.5. Zoom on the Second Positive Storm in the Asian Region

Figures 6a–6c show the VTEC maps at ~3.8 UT (a), at ~5:30 UT (b), and at ~7.25 UT (c) on 23 June 2015, when the second dayside positive storm began to develop (a), reached the maximum (b), and began to diminish (c).

One can see that during the disturbance maximum, the absolute VTEC reached 50–60 TECU around the magnetic equator and at low latitudes in the Southern Hemisphere. This positive effect was especially strong over Australia. Similar increase over the Asian sector was previously demonstrated in the data of SWA and of C/NOFS satellites at altitudes ~400–460 km (Figure 5).

It is interesting to note that during this positive storm the Defense Meteorological Satellite Program (DMSP) F15 satellite crossed the area several times (equatorial crossing at 14.7 LT). Figure 6d shows storm-to-quiet values of the ion density dNi calculated from the in situ measurements at the altitude of ~850 km. Data for 20 June 2015 are taken as the reference quiet-time values. One can see no storm time enhancement on the rightmost track (from 1.9 UT to 2.5 UT). From 3.6 UT to 4.2 UT the ion density at ~850 km of altitude increased by ~0.12×10^6 cm^{-3} in the SH, while in the NH the dNi showed much smaller storm time deviations. The time of this track is close to the time of the VTEC map presented in Figure 6a. During the next daytime passage from 5.3 UT to 5.9 UT, the DMSP measurements revealed more significant dNi deviation of ~0.15×10^6 cm^{-3} over north Australia and Indonesia, that is, also hemispherically asymmetric. It should be noted that the dNi enhancements correspond to an increase of the concentration of the O+ ions (not shown as a separate figure). This is the maximum of the positive storm as shown in VTEC maps in Figure 6b. From ~7 UT the dNi in the SH decreased to ~0.05×10^6 cm^{-3}, which is close to the quiet-time levels. It is interesting to note that the VTEC maps at ~7.25 UT still showed ~50–55 TECU enhancement. It is interesting to note that the results presented by Singh and Sripathi (2017) indicated the TEC enhancement over southern EIA over the Indian sector when we observe ion density and VTEC enhancements over the Asian region.

As mentioned above, the observed hemispheric asymmetry is most likely due to the seasonal effect of thermospheric winds, which in summer hemisphere can propagate to lower latitudes, while transporting a "composition disturbance zone" of increased mean molecular mass from high latitudes. Indeed, during the June 2015 storm data of thermospheric O/N2 ratio measured from ~2 to ~9 UT on 23 June by the Global Ultraviolet Imager (GUVI) on board the Thermosphere, Ionosphere, Mesosphere Energetics and Dynamics (TIMED) satellite show hemispherical asymmetry (Figure 6f). One can see that around ~180° longitude (equatorial crossing at 2:49 UT) O/N2 ratio is quite depleted at high and middle latitudes, while it is increased over low latitudes in SH. The composition bulge is concentrated over Northern Australia and Indonesia. Overall, comparison of Figures 6a–6c and 6f shows that the maximum VTEC enhancement is observed exactly over the area of the increased O/N2 ratio. Neutral composition changes have an important impact on the ionospheric distribution during geomagnetic storms. It is known that ionospheric ion density loss is proportional to the molecular concentration, so that an increase of the molecular mass causes a negative storm, while a decrease in the mean molecular mass provokes an increase in the ionospheric density (e.g., Fuller-Rowell et al., 1994).

The horizontal ion flows measured by C/NOFS (Figure 6e) confirm that the observed second positive storm was largely impacted by the thermosphere. One can see that at ~2.56–3.38 UT both meridional winds (Vy, shown in arrows) and zonal (Vx, shown in color) were quite small. At ~4.5 UT, the enhancement of southward winds are observed over Indonesia, and at ~ ~6.3–6.4 UT one can see ~80–100 m/s southward winds over eastern Australia and western Pacific Ocean. At ~6.6 UT, one can also observe enhancement of the eastward winds over Pacific Ocean.

It should be noted that the second positive phase of the 22–23 June 2015 storm was not reproduced correctly by most comprehensive first-principles models, such as SAMI3/RCM (results presented in Astafyeva et al., 2017), CTIPe, GITM, TIE-GCM (simulation results for this storm are available at https://ccmc.gsfc.nasa.gov/). Therefore, once again, our knowledge remains insufficient and more studies of ionospheric response to geomagnetic storms are necessary to improve our understanding of the ionospheric effects during geomagnetic storms.

3. Summary and Conclusions

In this work, we used data from ground-based magnetometers, ionosondes, maps of GPS-derived VTEC along with data from satellite missions Swarm, C/NOFS, DMSP, and GUVI, and we investigated electrodynamic and ionospheric behavior during the June 2015 major geomagnetic storm. We focused on effects at equatorial and low latitudes in American and Asian sectors. Below is the development of the storm as we conclude it from our results.

The storm started at 18:38 UT on 22 June 2015 and caused an immediate intensification of the equatorial eastward EF and the upward E × B drift on the dayside, which led to rapid strong enhancement of the VTEC and electron/ion density on the dayside. Concurrently, on the nightside, we observed downward vertical drift with decrease in the VTEC and plasma density. These effects started to diminish ~45–50 min after the storm commencement, when the IMF Bz turned northward, presuming penetration of the westward EF on the dayside and eastward EF on the nightside. During this period of time, both ground-based and spaceborne instruments showed that the EEJ changed sign from eastward to westward (CEJ). The equatorial westward EF was responsible for gradual decrease of the initial positive storm on the dayside by ~0–2 UT on 23 June. Our results showed that during the first several hours of the storm, the EEJ behavior corresponded to the IEF Ey variations, which led us to conclusion on the dominant role of the PPEF.

Starting from ~2 UT on 23 June 2015, the IMF Bz turned and remained southward until 5:50 UT. Interestingly, at this stage of the storm much less correlation between the IMF Bz and the electrodynamics was observed. On the nightside (in the American sector), small negative storm was observed in VTEC in the NH. On the dayside (Asian sector), there occurred several rapid fluctuations in the dH/EEJ and in the vertical plasma drift, which is, most likely, because of the eastward PPEF competing with the westward DDEF. However, despite the absence of significant upward plasma drift, the ionospheric ion/electron density and VTEC strongly increased over the whole dayside region from 2 to 6 UT on 23 June. Our multi-instrumental analysis demonstrates that the second positive ionospheric storm was significantly impacted by the thermosphere, including thermospheric winds and thermospheric composition.

Acknowledgments

We acknowledge the NASA/GSFC's Space Physics Data Facility's OMNIWeb service for the data of the interplanetary and geophysical parameters, and the OpenMadrigal web-service (http://cedar.openmadrigal.org) for the VTEC data used in this work. We thank the Bureau Central de Magnétisme Terrestre (BCMT, www.bcmt.fr) for the data of the magnetic observatory MBO and the magnetic station SAM. MBO is operated by the IPGP in collaboration with IRD and is funded by the CNRS INSU. Station SAM belongs to the WAMNET that is funded by the French Space Agency (CNES). We thank E. Yizengaw, E. Zesta, M. B. Moldwin, and the rest of the AMBER and SAMBA team for the data of magnetometers BANG and PUKT (http://magnetometers.bc.edu/index.php/78-magnetometers/78-home). AMBER is operated by Boston College and funded by the NASA and the AFOSR. Magnetometer stations LETI and PUER belong to the Low-Latitude Ionospheric Network (LISN) and their data are available from http://lisn.igp.gob.pe. LISN is a project led by the University of Texas at Dallas in collaboration with the Geophysical Institute of Peru and other institutions that provide information for the benefit of the scientific community. We acknowledge the Global Ionospheric Radio Observatory (GIRO, http://giro.uml.edu) for the data of the Jicamarca and Guam ionosonde stations. Data from Sao Luis ionosonde are available through the EMBRACE program from the National Institute for Space Research (INPE). DMSP data are available from the NGDC NOAA (https://satdat.ngdc.noaa.gov/dmsp/). GUVI data are available from http://guvitimed.jhuapl.edu/data_products. Data from BCL ionosonde station (SEALION network) are available on request from K. Hozumi (kukkai@nict.go.jp). We thank the University of Texas in Dallas for the data of the CINDI instrument onboard C/NOFS. We acknowledge the support of the Swarm mission from the European Space Agency (ESA); the Swarm mission data can be obtained from the ESA's EarthNet web services (http://earth.esa.int/swarm). We thank the Community Coordinated Modeling Center (CCMC, https://ccmc.gsfc.nasa.gov/) for runs on request by the CTIPe, GITM, and TIE-GCM models for the June 2015 storm. The results presented in this paper rely on geomagnetic indices calculated and made available by ISGI-Collaborating-Institutes (WDC for Geomagnetism—Kyoto, Japan; GFZ, Germany; EOST, France) from data collected at magnetic observatories. We thank the involved national institutes, the INTERMAGNET network, and International Service of

References

Abdu, M. A., Souza, J. R., Batista, I. S., Fejer, B. G., & Sobral, J. H. A. (2013). Sporadic E layer development and disruption at low latitudes by prompt penetration electric fields during magnetic storms. *Journal of Geophysical Research: Space Physics*, *118*, 2639–2647. https://doi.org/10.1002/jgra.50271

Alken, P., Chulliat, A., & Maus, S. (2013). Longitudinal and seasonal structure of the ionospheric equatorial electric field. *Journal of Geophysical Research: Space Physics*, *118*, 1298–1305. https://doi.org/10.1029/2012JA018314

Alken, P., Maus, S., Chulliat, A., Vigneron, P., Sirol, O., & Hulot, G. (2014). Swarm equatorial electric field chain: First results. *Geophysical Research Letters*, *42*, 673–680. https://doi.org/10.1002/2014GL062658

Alken, P., Maus, S., Vigneron, P., Sirol, O., & Hulot, G. (2013). Swarm SCARF equatorial electric field inversion chain. *Earth, Planets and Space*, *65*(11), 1309–1317. https://doi.org/10.5047/eps.2013.09.008

Anderson, D., Anghel, A., Chau, J. L., & Yumoto, K. (2006). Global, low-latitude, vertical E×B drift velocities inferred from daytime magnetometer observations. *Space Weather*, *4*, S08003. https://doi.org/10.1029/2005SW000193

Anderson, D., Anghel, A., Yumoto, K., Ishitsuka, M., & Kudeki, E. (2002). Estimating daytime vertical E×B drift velocities in the equatorial *F*-region using ground-based magnetometer observations. *Geophysical Research Letters*, *29*(12), 1596. https://doi.org/10.1029/2001GL014562

Astafyeva, E. (2009a). Effects of strong IMF Bz southward events on the equatorial and mid-latitude ionosphere. *Annales Geophysicae*, *27*(3), 1175–1187. https://doi.org/10.5194/angeo-27-1175-2009

Astafyeva, E. I. (2009b). Dayside ionospheric uplift during strong geomagnetic storms as detected by the CHAMP, SAC-C, TOPEX and Jason-1 satellites. *Advances in Space Research*, *43*(11), 1749–1756. https://doi.org/10.1016/j.asr.2008.09.036

Astafyeva, E., Zakharenkova, I., & Alken, P. (2016). Prompt penetration electric fields and the extreme topside ionospheric response to the 22–23 June 2015 geomagnetic storm as seen by the Swarm constellation. *Earth, Planets and Space*, *68*(1), 152. https://doi.org/10.1186/s40623-016-0526-x

Astafyeva, E., Zakharenkova, I., & Doornbos, E. (2015). Opposite hemispheric asymmetries during the ionospheric storm of 29–31 August 2004. *Journal of Geophysical Research: Space Physics*, *120*, 697–714. https://doi.org/10.1002/2014JA020710

Astafyeva, E., Zakharenkova, I., & Foerster, M. (2015). Ionospheric response to the 2015 St. Patrick's Day storm: A global multi-instrumental overview. *Journal of Geophysical Research: Space Physics*, *120*, 9023–9037. https://doi.org/10.1002/2015JA021629

Astafyeva, E., Zakharenkova, I., Huba, J. D., Doornbos, E., & van den IJssel, J. (2017). Global ionospheric and thermospheric effects of the June 2015 geomagnetic disturbances: Multi-instrumental observations and modeling. *Journal of Geophysical Research: Space Physics*, *122*, 11,716–11,742. https://doi.org/10.1002/2017JA024174

Blanc, M., & Richmond, A. D. (1980). The ionospheric disturbance dynamo. *Journal of Geophysical Research*, *85*, 1669–1686. https://doi.org/10.1029/JA085iA04p01669

de La Beaujardiere, O., Retterer, J. M., Pfaff, R. F., Roddy, P. A., Roth, C., Burke, W. J., et al. (2009). C/NOFS observations of deep plasma depletions at dawn. *Geophysical Research Letters*, *36*, L00C06. https://doi.org/10.1029/2009GL038884

Fejer, B. G. (1981). The equatorial ionospheric electric field. A review. *Journal of Atmospheric and Terrestrial Physics*, *43*(5-6), 377–386. https://doi.org/10.1016/0021-9169(81)90101-X

Fejer, B. G. (2002). Low latitude storm time ionospheric electrodynamics. *Journal of Atmospheric and Solar - Terrestrial Physics*, *64*(12-14), 1401–1408. https://doi.org/10.1016/S1364-6826(02)00103-7

Fejer, B. G., Gonzales, C. A., Farley, D. T., Kelley, M. C., & Woodman, R. F. (1979). Equatorial electric fields during magnetically disturbed conditions. 1. Effect of the interplanetary magnetic field. *Journal of Geophysical Research*, *84*(A10), 5797–5802. https://doi.org/10.1029/JA084iA10p05797

Fuller-Rowell, T. J. (2011). Storm-time response of the thermosphere-ionosphere system. In M. A. Abdu, D. Pancheva, & A. Bhattacharyya (Eds.), *Aeronomy of the Earth's Atmosphere and Ionosphere*, *IAGA Spec. Sopron Book Ser.* (Vol. 2, pp. 419–435). Dordrecht, Netherlands: Springer. https://doi.org/10.1007/978-94-007-0326-1

Geomagnetic Indices (isgi.unistra.fr). E. A. acknowledges the support of the European Research Council (ERC, grant agreement 307998). I. Z. is supported in part by the Russian Foundation for Basic Research (RFBR) grant 16-05-01077. P. C. acknowledges the support of the French National Space Agency (CNES). The work of M. R. H. and W. R. C. is sponsored by NSF grant AGS-1552245 and NASA grant NNX-15AT31G. The figures are done by using the Generic Mapping Tools (GMT) software (http://gmt.soest.hawaii.edu). We thank Tim Fuller-Rowell (NOAA) and Kumiko Hashimoto (Kubi International University) for fruitful discussions. This is IPGP contribution 3927.

Fuller-Rowell, T. J., Codrescu, M. V., Moffett, R. J., & Quegan, S. (1994). Response of the thermosphere and ionosphere to geomagnetic storms. *Journal of Geophysical Research*, *99*(A3), 3893–3914. https://doi.org/10.1029/93JA02015

Fuller-Rowell, T. J., Millward, G. H., Richmond, A. D., & Codrescu, M. V. (2002). Storm-time changes in the upper atmosphere at low-latitudes. *Journal of Atmospheric and Solar - Terrestrial Physics*, *64*(12-14), 1383–1391. https://doi.org/10.1016/S1364-6826(02)00101-3

Goncharenko, L. P., Foster, J. C., Coster, A. J., Huang, C., Aponte, N., & Paxton, L. J. (2007). Observations of a positive storm phase on September 10, 2005. *Journal of Atmospheric and Solar - Terrestrial Physics*, *69*(10-11), 1253–1272. https://doi.org/10.1016/j.jastp.2006.09.011

Hairston, M., Coley, W. R., & Stoneback, R. (2013). Vertical and meridional equatorial ion flows observed by CINDI during the 26 September 2011 storm. *Journal of Geophysical Research: Space Physics*, *118*, 5230–5243. https://doi.org/10.1002/jgra.50411

Hairston, M., Coley, W. R., & Stoneback, R. (2016). Responses in the polar and equatorial ionosphere to the March 2015 St. Patrick Day storm. *Journal of Geophysical Research: Space Physics*, *121*, 11,213–11,234. https://doi.org/10.1002/2016JA023165

Heelis, R. A. (2004). Electrodynamics in the low and middle latitude ionosphere: A tutorial. *Journal of Atmospheric and Solar - Terrestrial Physics*, *66*(10), 825–838. https://doi.org/10.1016/j.jastp.2004.01.034

Huang, C.-M. (2013). Disturbance dynamo electric fields in response to geomagnetic storms occurring at different universal times. *Journal of Geophysical Research: Space Physics*, *118*, 496–501. https://doi.org/10.1029/2012JA018118

Huang, C.-S., Foster, J. C., & Kelley, M. C. (2005). Long-duration penetration of the interplanetary electric field to the low-latitude ionosphere during the main phase of magnetic storms. *Journal of Geophysical Research*, *110*, A11309. https://doi.org/10.1029/2005JA011202

Huang, C.-S., Sazykin, S., Chau, J. L., Maruyama, N., & Kelley, M. C. (2007). Penetration electric fields: Efficiency and characteristic time scale. *Journal of Atmospheric and Solar - Terrestrial Physics*, *69*(10-11), 1135–1146. https://doi.org/10.1016/j.jastp.2006.08.016

Huang, C.-S., Wilson, G. R., Hairston, M. R., Zhang, Y., Wang, W., & Liu, J. (2016). Equatorial ionospheric plasma drifts and O+ concentration enhancements associated with disturbance dynamo during the 2015 St. Patrick's Day magnetic storm. *Journal of Geophysical Research: Space Physics*, *121*, 7961–7973. https://doi.org/10.1002/2016JA023072

Kelley, M. C., Fejer, B. G., & Gonzales, C. A. (1979). An explanation for anomalous equatorial ionospheric electric fields associated with a northward turning of the interplanetary magnetic field. *Geophysical Research Letters*, *6*(4), 301–304. https://doi.org/10.1029/GL006i004p00301

Kikuchi, T., & Hashimoto, K. K. (2016). Transmission of the electric fields to the low latitude ionosphere in the magnetosphere-ionosphere current circuit. *Geoscience Letters*, *3*(1), 1–11. https://doi.org/10.1186/s40562-016-0035-6

Kikuchi, T., Hashimoto, K. K., & Nozaki, K. (2008). Penetration of magnetospheric electric fields to the equator during a geomagnetic storm. *Journal of Geophysical Research*, *113*, A06214. https://doi.org/10.1029/2007JA012628

Kikuchi, T., Pinnock, M., Rodger, A., Lühr, H., Kitamura, T., Tachihara, H., et al. (2000). Global evolution of a substorm-associated DP2 current system observed by superDARN and magnetometers. *Advances in Space Research*, *26*(1), 121–124. https://doi.org/10.1016/S0273-1177(99)01037-6

Kuai, J., Liu, L., Liu, J., Sripathi, S., Zhao, B., Chen, Y., et al. (2016). Effects of disturbed electric fields in the low-latitude and equatorial ionosphere during the 2015 St. Patrick's day storm. *Journal of Geophysical Research: Space Physics*, *121*, 9111–9126. https://doi.org/10.1002/2016JA022832

Lin, C. H., Richmond, A. D., Bailey, G. J., Liu, J. Y., Lu, G., & Heelis, R. A. (2009). Neutral wind effect in producing a storm time ionospheric additional layer in the equatorial ionization anomaly region. *Journal of Geophysical Research*, *114*, A09306. https://doi.org/10.1029/2009JA014050

Lu, G., Goncharenko, L. P., Richmond, A. D., Roble, R. G., & Aponte, N. (2008). A dayside ionospheric positive storm phase driven by neutral winds. *Journal of Geophysical Research*, *113*, A08304. https://doi.org/10.1029/2007JA012895

Mannucci, A. J., Tsurutani, B. T., Lijima, B. A., Komjathu, A., Saito, A., Gonzalez, W. D., et al. (2005). Dayside global ionospheric response to the major interplanetary events of October 29–30, 2003 "Halloween storms". *Geophysical Research Letters*, *32*, L12S02. https://doi.org/10.1029/2004GL021467

Manoj, C., Maus, S., Luehr, H., & Alken, P. (2008). Penetration characteristics of the interplanetary electric field to the daytime equatorial ionosphere. *Journal of Geophysical Research*, *113*, A12310. https://doi.org/10.1029/2008JA013381

Manoj, C., Maus, S., & Alken, P. (2013). Long-period prompt-penetration electric fields derived from CHAMP satellite magnetic measurements. *Journal of Geophysical Research: Space Physics*, *118*, 5919–5930. https://doi.org/10.1002/jgra.50511

Maruyama, N., Richmond, A. D., Fuller-Rowell, T. J., Codrescu, M. V., Sazykin, S., Toffoletto, F. R., et al. (2005). Interaction between direct penetration and disturbance dynamo electric fields in the storm-time equatorial ionosphere. *Geophysical Research Letters*, *32*, L17105. https://doi.org/10.1029/2005GL023763

Nishida, A. (1968). Geomagnetic *DP2* fluctuations and associated magnetospheric phenomena. *Journal of Geophysical Research*, *73*(5), 1795–1803. https://doi.org/10.1029/JA073i005p01795

Paznukhov, V. V., Reinisch, B. W., Song, P., Huang, X., Bullett, T. W., & Veliz, O. (2007). Formation of an F3 layer in the equatorial ionosphere: A result from strong IMF changes. *Journal of Atmospheric and Solar - Terrestrial Physics*, *69*(10-11), 1292–1304. https://doi.org/10.1016/j.jastp.2006.08.019

Paznukhov, V. V., Altadil, D., & Reinisch, B. W. (2009). Experimental evidence for the role of the neutral wind in the development of ionospheric storms in mid-latitudes. *Journal of Geophysical Research*, *114*, A12319. https://doi.org/10.1029/2009JA014479

Ramsingh, S., Sripathi, S., Sreekumar, S., Banola, K., Emperumal, P. T., & Kumar, B. S. (2015). Low-latitude ionosphere response to super geomagnetic storm of 17/18 March 2015: Results from a chain of ground based observations over Indian sector. *Journal of Geophysical Research: Space Physics*, *120*, 10,864–10,882. https://doi.org/10.1002/2015JA021509

Rastogi, R. G. (1989). The equatorial electrojet, magnetic and ionospheric effects. In J. Jacobs (Ed.), *Geomagnetism* (Vol. 3, pp. 461–525). San Diego, CA: Academic.

Rastogi, R. G. (2006). Magnetic storm effects at equatorial electrojet stations. *Earth, Planets and Space*, *58*(5), 645–657. https://doi.org/10.1186/BF03351962

Rastogi, R. G., Chandra, H., & Chakrabarty, S. C. (1971). The disappearance of equatorial Es and the reversal of electrojet current. *Proceedings of the Indiana Academy of Sciences*, *74*(2), 62–67. https://doi.org/10.1007/BF03047392

Reinisch, B. W., & Galkin, I. A. (2011). Global ionospheric radio observatory (GIRO). *Earth, Planets and Space*, *63*(4), 377–381. https://doi.org/10.5047/eps.2011.03.001

Reinisch, B. W., Scali, J. L., & Haines, D. M. (1998). Ionospheric drift measurements with ionosondes. *Annali di Geofisica*, *41*(5–6), 695–702.

Rideout, W., & Coster, A. (2006). Automated GPS processing for global total electron content data. *GPS Solutions*, *10*(3), 219–228. https://doi.org/10.1007/s10291-006-0029-5

Scherliess, L., & Fejer, B. (1997). Storm-time dependence of equatorial disturbance dynamo zonal electric fields. *Journal of Geophysical Research*, *102*(A11), 24,037–24,046. https://doi.org/10.1029/97JA02165

Singh, R., & Sripathi, S. (2017). Ionospheric response to 22–23 June 2015 storm as investigated using ground-based ionosondes and GPS receivers over India. *Journal of Geophysical Research: Space Physics*, *122*, 11,645–11,664. https://doi.org/10.1002/2017JA024460

Tsurutani, B., Mannucci, A., Lijima, B., Ali Abdu, M., Sobral, J. H. A., Gonzalez, W., et al. (2004). Global dayside ionospheric uplift and enhancement associated with interplanetary electric fields. *Journal of Geophysical Research*, *109*, A08302. https://doi.org/10.1029/2003JA010342

Tsurutani, B. T., Verkhoglyadova, O. P., Mannucci, A. J., Saito, A., Araki, T., Yumoto, K., et al. (2008). Prompt penetration electric fields (PPEFs) and their ionospheric effects during the great magnetic storm of 30–31 October 2003. *Journal of Geophysical Research*, *113*, A05311. https://doi.org/10.1029/2007JA012879

Tulasi Ram, S., Yokoyama, T., Otsuka, Y., Shiokawa, K., Sripathi, S., Veenadhari, B., et al. (2016). Duskside enhancement of equatorial zonal electric field response to convection electric fields during the St. Patrick's Day storm on 17 March 2015. *Journal of Geophysical Research: Space Physics*, *121*, 538–548. https://doi.org/10.1002/2015JA021932

Valladares, C. E., & Chau, J. L. (2012). The low-latitude ionosphere sensor network: Initial results. *Radio Science*, *47*, RS0L17. https://doi.org/10.1029/2011RS004978

Venkatesh, K., Tulasi Ram, S., Fagundes, P. R., Seemala, G. K., & Batista, I. S. (2017). Electrodynamic disturbances in the Brazilian equatorial and low-latitude ionosphere on St. Patrick's day storm of 17 march 2015. *Journal of Geophysical Research: Space Physics*, *122*, 4553–4570. https://doi.org/10.1002/2017JA024009

Verkhoglyadova, O. P., Tsurutani, B. T., Mannucci, A. J., Mlynczak, M. G., Hunt, L. A., Paxton, L. J., & Komjathy, A. (2016). Solar wind driving of ionosphere-thermosphere responses in three storms near St. Patrick's Day in 2012, 2013, and 2015. *Journal of Geophysical Research: Space Physics*, *121*, 8900–8923. https://doi.org/10.1002/2016JA022883

World Data Center for Geomagnetism, Kyoto, Nose, M., Iyemori, T., Sugiura, M., & Kamei, T. (2015a). Geomagnetic Dst index. https://doi.org/10.17593/14515-74000

World Data Center for Geomagnetism, Kyoto, Nose, M., Iyemori, T., Sugiura, M., & Kamei, T. (2015b). Geomagnetic AE index. https://doi.org/10.17593/15031-54800

Yamazaki, Y., & Kosch, M. J. (2015). The equatorial electrojet during geomagnetic storms and substorms. *Journal of Geophysical Research: Space Physics*, *120*, 2276–2287. https://doi.org/10.1002/2014JA020773

Yizengaw, E., & Moldwin, M. B. (2009). African Meridian B-field Education and Research (AMBER) Array. *Earth, Moon, and Planets*, *104*(1-4), 237–246. https://doi.org/10.1007/s11038-008-9287-2

Yizengaw, E., Zesta, E., Moldwin, M. B., Damtie, B., Mebrahtu, A., Valladares, C. E., & Pfaff, R. F. (2012). Longitudinal differences of ionospheric vertical density distribution and equatorial electrodynamics. *Journal of Geophysical Research*, *117*, A07312. https://doi.org/10.1029/2011JA017454

Yizengaw, E., Moldwin, M. B., Zesta, E., Biouele, C. M., Damtie, B., Mebrahtu, A., et al. (2014). The longitudinal variability of equatorial electrojet and vertical drift velocity in the African and American sectors. *Annales de Geophysique*, *32*(3), 231–238. https://doi.org/10.5194/angeo-32-231-2014

Zakharenkova, I., Astafyeva, E., & Cherniak, I. (2016). GPS and GLONASS observations of traveling ionospheric disturbances during the 2015 St. Patrick's Day storm. *Journal of Geophysical Research: Space Physics*, *121*, 12,138–12,156. https://doi.org/10.1002/2016JA023332

Zhao, B., Wan, W., & Liu, L. (2005). Responses of equatorial anomaly to the October – November 2003 superstorms. *Annales de Geophysique*, *23*(3), 693–706. https://doi.org/10.5194/angeo-23-693-2005